RF Safety Evaluation of a Breast Tissue Expander Device for MRI: Numerical Simulation and Experiment

Bu S. Park, Amir Razjouyan, Leonardo M. Angelone, Brent McCright, and Sunder S. Rajan

***Abstract*—This study describes the MRI-related radio frequency (RF) safety evaluation of breast tissue expander devices to establish safety criteria. Numerical simulations and experimental measurements were performed at 64 MHz with a gel phantom containing a breast expander. Additionally, computational modeling was performed (64 and 128 MHz) with an adult female model, containing a virtually implanted breast tissue expander device for four imaging landmark positions. The presence of the breast tissue expander device led to significant alterations in specific absorption rate (SAR) and $|B_1^+|$ distributions. The main source of SAR alterations with the use of the breast expander device was the saline-filled pouch of the expander. Conversely, the variation of RF magnetic field (B_1^+) was mainly caused by the metallic port. The measured values of electric field magnitude did not increase significantly due to the introduction of the expander device. The maximum 1g- or 10g-averaged SAR values in tissues near the implant were lower than those expected in other regions of the patient body with normalization of both $|B_1^+|$ equal to 2 μT at the coil isocenter and whole body averaged SAR equal to 4 W/kg.**

***Index Terms*—Computational modeling, finite difference time domain (FDTD), landmarks, specific absorption rate (SAR), women's health.**

I. Introduction

THE American Cancer Society estimated that there are more than 250 000 new cases of breast cancer every year in the US [1]. Postmastectomy breast reconstruction is usually accomplished using tissue expanders and is a common technique used for breast reconstruction. According to a study published in 2003 involving 1984 breast cancer subjects, approximately 49% of the subjects underwent mastectomies [2]. This has resulted in a significant number of breast tissue expanders being used. Although the precise number of such devices in use is not available, the Food and Drug Administration (FDA) database indicates that more than 50 breast tissue expander devices have been cleared through the FDA 510(k) process [3].

Manuscript received November 25, 2016; revised February 3, 2017; accepted March 1, 2017. This work was supported by the FDA Office of Women Health (OWH) Program. *(Corresponding author: Sunder S. Rajan.)*

B. S. Park and B. McCright are with the U.S. FDA, CBER, OTAT Division of Cellular and Gene Therapies, Silver Spring, MD 20993-0002 USA (e-mail: bu.park@fda.hhs.gov; Brenton.McCright@fda.hhs.gov).

L. M. Angelone, A. Razjouyan, and S. S. Rajan are with the U.S. FDA, CDRH, OSEL, Division of Biomedical Physics, Silver Spring, MD 20993-0002 USA (e-mail: Leonardo.Angelone@fda.hhs.gov; Amir.Razjouyan@fda.hhs.gov; sunder.rajan@fda.hhs.gov).

Color versions of one or more of the figures in this paper are available online at http://ieeexplore.ieee.org.

Digital Object Identifier 10.1109/TEMC.2017.2678201

Patients with breast tissue expanders sometimes need to be imaged by MRI for follow-up. However, there are unresolved safety concerns pertaining to the use of these devices in the MR environment. Due to the absence of MR conditional labeling for these devices that have been previously cleared, the MRI scanning of patients with these devices is potentially an off-label practice and the safety concerns need to be better understood and disseminated.

Breast tissue expanders are composed of a bladder (i.e., elastomer wall), with silicone outer shells and either an internal valve or external metallic port to allow for saline fluid injections. Typically, a small permanent magnet is embedded inside the metallic port to locate the injection slot for additional saline injections. After the pouch is implanted, it is then gradually expanded over a few weeks with periodic saline injections through the port. When the target size is reached, the device is eventually replaced with a permanent breast implant.

The presence of the metallic port and the magnet contained in the device raises possible safety concerns in the MRI environment related to radio frequency (RF) induced heating of tissue, gradient-induced heating, and effects of mechanical forces and torque on the device [4]. The presence of metal can also generate significant image artifacts, which can in turn lead to the loss of diagnostic utility of the images. Thus, a careful development and evaluation of the effects of the MRI environment is needed for breast tissue expanders used in mastectomy patients.

Recently, Nava *et al.* [5] have studied the forces generated in four samples by the static magnetic field on the breast tissue expander implant due to the presence of a permanent magnet within the implant body. The study found significant attractive forces (>60° deflection) using a 1.5 T system. These results are similar to results observed in our work [6]. Despite these results, Nava *et al.* concluded that "under selected conditions, MRI can be feasible," which raises the potential for off-label use. Additionally, the study included infrared image data of heating on the surface of a tissue-mimicking-gelled saline phantom containing a breast tissue expander device based on the ASTM standard F2182-09 and stated that "heating is not expected to be a major concern." However, RF-induced heating is strongly spatially dependent and as such there is the concern that measurements on the surface of the phantom may have not fully captured the possible RF-induced heating in the region surrounding the breast expander.

The goal of this study is to re-examine the possible concerns of RF safety with a breast expander during an MRI scan. During an MRI scan, the use of RF pulses lead to deposition of energy in the subject, through electric field coupling and induced eddy currents in the body [7], [8]. The energy dissipated in the patient during the scan is assessed in terms of specific absorption rate (SAR), which is defined as the amount of power absorbed per unit mass of tissue [8], [9]. When metallic implants are present in the body, the currents induced in the implants can generate a significant increase in local SAR, and related temperature in the surrounding tissue [10]–[14]. In addition, the large volume of embedded dielectric material also has the potential to alter surrounding electric fields [15].

Although there have been numerous reports on the effect of small metallic passive devices on induced fields, the effects of a large device such as a breast implant filled with saline or silicone have not received much attention [16]. The aforementioned report by Nava *et al.* included a novel measurement of RF heating on breast expander devices using a variant of ASTM test standard. However, the use of an infrared camera limits the volume of evaluation to the surface of the phantom and cannot detect temperature changes deep inside the phantom [5]. In addition, the values of RF-induced heating measured in the ASTM phantom could differ significantly from *in vivo* conditions due to differences in local RF fields. Computational modeling offers a viable approach to both explore SAR effects all around the implanted device as well to look for effects in an anatomically accurate model. An anatomically precise computational model of an adult female subject was thus used in our study. Additionally, it is now evident from recent studies that patient positioning in the bore and RF coil design can also significantly alter the SAR maps, as shown by recent simulation studies [17], [18], hence the effect of positioning is also evaluated in this study.

II. Methods

The approach to this study is done by comparison of numerical and experimental of the RF safety evaluation of breast tissue expander devices in the ASTM phantom for in vitro study. This was done as a validation of the numerical simulation with the experimental results by looking at the electric and magnetic fields. Further analysis of the devices in an *in vivo* case was studied through numerical simulation. This is done to understand the energy absorbed within the tissues of the human cell in an RF MR environment.

A. Numerical Simulations

This study was performed by means of numerical simulations based on the finite difference time domain (FDTD) method [19], [20] and a computational model of an adult female subject [21]. The simulations were used to generate $\mathbf{B}_1^+$ and SAR [8], [9] distributions at 64 and 128 MHz (corresponding to 1.5 and 3.0 T MRI proton frequencies, respectively). The breast tissue expander device was filled with a generic saline, and was evaluated for the body model at four different landmark positions along the *Z*-axis, i.e., shoulder, heart, sternum, and abdomen. Each landmark position was named based on a location of the body coil centered in the *Z*-axis. For example, the heart landmark indicates that the center of the body coil is in line with the center of the heart in the *Z*-axis.

The analysis was also extended to a generic silicone-filled breast implant containing no metallic or magnetic components for comparison.

1) Computational Model of Breast Implants: A generic type of breast expander device (labeled as "expander"), including a full breast expander with a metallic port, an elastomer shell, and a filled saline pouch [see Fig. 1(c)], was modeled for this study. The "expander" was constructed based on physical product samples and was shaped as an oblong pouch within an elastomer shell, with major and minor axes of 108 and 82 mm, respectively, and thickness of 35 mm. The metallic port consisted of two cylindrical compartments, with the base diameter of 36 mm and height of 9 mm. The top portion had a diameter of 13.5 mm and height of 5 mm. The device also had two small holes with a 2 mm diameter, symmetrically placed on opposite sides for fluid control [yellow arrows in Fig. 1(c)]. The elastomer port cover has a base diameter of 44 mm, inner diameter (ID) of 36.5 mm, and height of 10 mm. The top portion containing a small samarium cobalt permanent magnet has an outer diameter of 26 mm, ID of 20 mm, and height of 3 mm.

The metallic compartment of the device [see Fig. 1(c)] was composed of a titanium needle guard containing a magnet and adhesive silicone. The conductivity (σ) and relative permittivity (ε_r) of the device materials were defined as follows: titanium ($\sigma = 2.33 \times 10^6$ S/ m, $\varepsilon_r = 1$), samarium-cobalt ($\sigma = 1.16 \times 10^6$ S/ m, $\varepsilon_r = 1$), saline ($\sigma = 0.47$ S/ m, $\varepsilon_r = 80$), high consistency silicone elastomer ($\sigma = 1.0 \times 10^{-3}$ S/ m, $\varepsilon_r = 3$), elastomer shell ($\sigma = 1.0 \times 10^{-13}$ S/ m, $\varepsilon_r = 1$) representing the range of variability depending on manufacturer [3], [22]. The positioning of the expander device in the breast region of an adult female human model is shown in Fig. 1(d). The device was located at the region of breast tissues without tissue morphing, assuming that the tissues were mostly removed after surgery of mastectomy. The electrical properties of the breast region were assigned as $\sigma = 0.029$ S/ m, $\varepsilon_r = 5.8$ at 64 MHz, and $\sigma = 0.030$ S/ m, $\varepsilon_r = 5.7$ at 128 MHz assuming fat is the dominant component of the region [23]. The closest distance between the device and the skin was about 0.9 cm in the *x*-axis, 0.5 cm in the *y*-axis, and 1.8 cm in the *z*-axis in this study. A device "volume-of-interest" (*VoI*) (see white rectangular box in Figs. 3–6) was defined as a $350 \times 300 \times 80$ mm^3 volume around the expander device. The center of the *VoI* was –1.3 cm off in the *x*-axis from the center of the device to improve the visibility of the device with respect to surrounding region.

Two additional configurations of the "expander" device were also modeled for additional analysis, namely: "metal only" which includes the metallic port and the elastomer shell, but without the saline, and "saline only," which includes the elastomer shell and the filled saline, but without the metallic port. Finally, a generic silicone-based breast implant of the same size but without a metallic port (labeled as "silicone") was also modeled for comparison. This model included the elastomer shell, as described above containing silicone (instead of saline), and no metallic components. The electrical properties of the silicone were $\sigma = 0.10$ S/ m, $\varepsilon_r = 11.7$. Simulations at 128 MHz were performed with five different conditions: 1) "no-implant,"

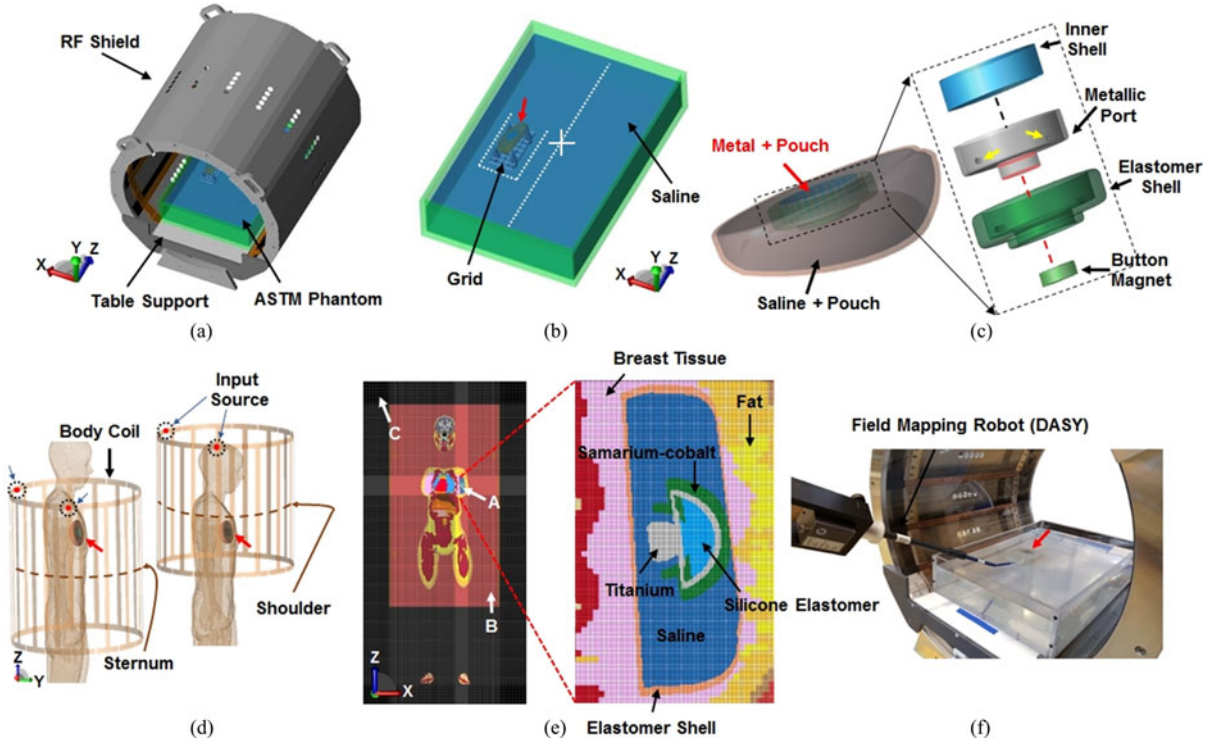

Fig. 1. Geometrical model used for the study. (a) Model of the RF coil and RF shield loaded with the ASTM phantom. (b) The ASTM phantom filled with a saline solution and loaded with the device (red arrow). The device is fixed in the grid (black arrow). White dotted lines indicate an approximate location of the transverse and sagittal planes where $||\mathbf{B_{xy}}||$ and $||\mathbf{E}||$ were measured and calculated. A white cross line indicates the location of an origin. (c) Model of the breast tissue expander device. The device contains metal (red arrow) and saline (black arrow). The size of the device can be altered using a saline injection port (yellow arrow). (d) Model of the 16-rod high-pass birdcage RF coil loaded with the anatomical female model ("Ella") and the device (red arrow). Two of the four landmark positions evaluated are shown: sternum (left) and shoulder (right). The location of input sources was shown. (e) Mesh used for the study. A multiresolution grid used for the simulations, with $0.5 \times 0.5 \times 0.5\,\mathrm{mm}^3$ (region A, including the device), $5 \times 5 \times 5\,\mathrm{mm}^3$ (region B, within the RF shield and Ella model), and $20 \times 20 \times 20\,\mathrm{mm}^3$ (region C, outside of the RF shield). (f) Experimental setup with the field mapping robot and the breast expander device (red arrow) for the measurements.

2) "expander," 3) "metal only," 4) "saline only," and 5) "silicone." Additionally, a sensitivity analysis with the "*silicone*" model was conducted with the ID of 610 mm body coil, using two different values of conductivity, i.e., $\sigma_1 = 0.1$ S/m and $\sigma_2 = 1$ S/m, which represent the range of variability for silicone, depending on manufacturer [3]. The SAR sensitivity was calculated as

$$\text{SAR Sensitivity} = 100 \times \left(\frac{\text{SAR}_{\sigma_2} - \text{SAR}_{\sigma_1}}{\text{SAR}_{\sigma_1}}\right) \Big/ (\sigma_2 - \sigma_1) \quad [\%/\,(\text{S/m})] \tag{1}$$

where SAR_{σ_1} and SAR_{σ_2} indicate the value of SAR (i.e., $\text{SAR}_{1\text{g}}$, or $\text{SAR}_{10\text{g}}$) calculated for σ_1 and σ_2, respectively, and normalized to $|\mathbf{B_1^+}| = 2\,\mu\text{T}$ at the center of the RF coil.

The SAR values after normalization of $|\mathbf{B_1^+}| = 2\,\mu\text{T}$ were calculated as

$$\text{SAR}_{\text{after}} = \left(\frac{2\,\mu\text{T}}{|\text{B}_1^+|_{\text{center}}}\right)^2 \times \text{SAR}_{\text{before}} \tag{2}$$

where $\text{SAR}_{\text{after}}$ and $\text{SAR}_{\text{before}}$ indicate the value of SAR after and before the normalization, and $|\text{B}_1^+|_{\text{center}}$ is the $|\mathbf{B_1^+}|$ at the center of the coil.

In this study, the geometrical size of the breast expander device was fixed to match the human model, i.e., "Ella," used in the numerical simulations. In clinical applications, the size of the device is typically adjusted to the patient's anatomy. However, two different filling conditions of the device, i.e., full vs. half-full [5], were used to evaluate the electromagnetic field variations at 64 MHz.

2) Computational Model of RF Coil: Three different geometries of a quadrature 16-rod high-pass birdcage body coil model were used to perform simulations at 64 and 128 MHz. The first coil model ("750 mm coil," 128 MHz) had an ID of 750 mm and with an RF shield (ID $= 825$ mm, $L = 850$ mm) [24]. The inner length of the coil (i.e., length without width of the end-ring rod) was 520 mm, whereas the outer length was 600 mm (MITS1.5, Zurich Med Tech, Zurich, Switzerland). The second coil model ("610 mm coil," 128 MHz) had an ID of 610 mm and an RF shield (ID= 660, $L = 1220$ mm), and inner vs. outer length of 570 vs. 620 mm, respectively [25]. The third coil model ("746 mm coil," 64 MHz) had an ID of 746 mm and an RF shield (ID= 827, $L = 845$ mm), and inner vs. outer length of 570 vs. 650 mm, respectively (see Table I).

Tuning capacitors were placed in the end-rings and have values of 74 pF (64 MHz/1.5T, 746 mm coil), 14 pF (128 MHz/3T, 750 mm coil), 16.5 pF (128 MHz/3T, 610 mm coil) [see Fig. 1(d]. Each coil was modeled assuming a fixed tuning condition to demonstrate applications for clinical condition and previous research [17], [18]. The variation of resonance frequency with addition of the breast expander device was tested and verified

TABLE I
RF COIL MODELS

	750 mm coil (3.0 T)	610 mm coil (3.0 T)	746 mm coil (1.5 T)
Inner diameter (ID) [mm]	750	610	746
Inner length [mm]	520	570	570
Outer length [mm]	600	620	650
Tuning capacitor [pF]	14	16.5	74
RF shield – ID [mm]	825	660	827
– Length [mm]	850	1220	845

to be minimal (e.g., with 610 mm coil at 3.0 T the resonance frequency was 127.98 MHz with the "expander" and 128.02 MHz without it) (see Table I).

Two input ports for each RF coil were used in numerical simulations. Each input port was set as a voltage source with a 50 Ω resistor in series, a sinusoidal waveform at 64 or 128 MHz, and phase of 0° or 90° to obtain a quadrature excitation [see Fig. 1(d)].

3) Computational Model of ASTM Phantom: A model of the ASTM phantom ("phantom"), based on the ASTM standard test method [26] [see Fig. 1(a) and (b)], was also used in this study. The dimensions of the phantom were 650 mm in length, 420 mm in width, and 90 mm in height. The electrical properties of the internal volume were $\sigma = 0.47\,\mathrm{S/m}$ and $\varepsilon_r = 80$.

4) Computational Model of Human Body: An adult female human model ("Ella," virtual family [21]) was used for the study (see Fig. 1). The model has 36 distinguished anatomical structures, with electrical properties assigned as in previous literature [23], [27]. Simulations were performed with the body model in four different landmark positions: shoulder, heart, and sternum [reference landmark, Fig. 1(d) and (e)], and abdomen. The offset of the landmarks along the *Z*-axis with respect to the reference was: −280 mm (shoulder), −145 mm (heart), and +165 mm (abdomen).

5) FDTD Numerical Implementation: A multiresolution grid with 0.5 × 0.5 × 0.5 mm^3 (region A, i.e., volume containing the device), 5 × 5 × 5 mm^3 (region B, volume within the RF shield including the body model), and 20 × 20 × 20 mm^3 (region C, volume outside the RF shield) was used in numerical simulations to minimize calculation time and memory requirements [see Fig. 1(e)]. The boundary conditions were set as 12 perfectly matching layers. The simulation results of multiresolution data were reconstructed using a two-dimensional (2-D)-linear interpolation method of a commercial software (MATLAB, the MathWorks, Inc., Natick, MA) and grid information of the simulation models [28]. All numerical simulations were reached the convergence threshold of −60 dB.

The numerical simulations were performed using the commercially available xFDTD software (Remcom, Inc.; State College, PA) and postprocessing analysis was performed in MATLAB (the MathWorks, Inc., Natick, MA). The simulation results were normalized using two different approaches: 1) whole body averaged SAR ($\mathrm{SAR_{WB}}$) equal to 4 W/kg (first-level-controlled operating mode [9], or 2) $|\mathbf{B_1^+}|$ equal to 2 μT at the coil single-voxel isocenter corresponding to a 90° flip angle of a 3 ms rectangular RF pulse [28].

The magnitude of $\mathbf{B_1^+}$ ($|\mathbf{B_1^+}|$), $\mathrm{SAR_{WB}}$, 1g-averaged SAR ($\mathrm{SAR_{1g}}$) and 10g-averaged SAR ($\mathrm{SAR_{10g}}$) over the volume of interest were computed, where $\mathrm{SAR_{1g}}$ refers to the average value of SAR in a 1 g region of tissue surrounding the voxel and similarly for $\mathrm{SAR_{10g}}$. The difference of $|\mathbf{B_1^+}|$ ($\Delta|\mathbf{B_1^+}|$) with and without the "expander" was calculated pixel wise as

$$\Delta\left|\mathbf{B_1^+}\right| = \frac{\left|\mathbf{B_1^+}\right|_{\mathrm{With}} - \left|\mathbf{B_1^+}\right|_{\mathrm{Without}}}{\mathrm{mean}\left(\left|\mathbf{B_1^+}\right|_{\mathrm{Without}}\right)} \times 100\ [\%] \qquad (3)$$

where mean $|\mathbf{B_1^+}|_{\mathrm{without}}$ is the mean value of $|\mathbf{B_1^+}|$ over the volume of interest without the breast expander device.

The differences of $\mathrm{SAR_{1g}}$ and $\mathrm{SAR_{10g}}$ with and without the device were calculated as

$$\begin{cases} \Delta\mathrm{SAR_{1g}} = \dfrac{\mathrm{SAR_{1g-with} - SAR_{1g-without}}}{\mathrm{mean\ SAR_{1g-without}}} \times 100\ [\%] \\ \Delta\mathrm{SAR_{10g}} = \dfrac{\mathrm{SAR_{10g-with} - SAR_{10g-without}}}{\mathrm{mean\ SAR_{10g-without}}} \times 100\ [\%] \end{cases} \qquad (4)$$

where $\mathrm{mean\ SAR_{1g-without}}$ and $\mathrm{mean\ SAR_{10g-without}}$ are the mean value of $\mathrm{SAR_{1g}}$ and $\mathrm{SAR_{10g}}$, respectively, over the volume of interest without the device

The difference of peak $\mathrm{SAR_{1g}}$ ($\mathrm{SAR_{1g-peak}}$), and $\mathrm{SAR_{10g-peak}}$ with and without the device was calculated as

$$\Delta\mathrm{SAR_{Peak}} = \frac{\mathrm{SAR_{Peak-with} - SAR_{Peak-without}}}{\mathrm{SAR_{Peak-without}}} \times 100\ [\%]\,. \qquad (5)$$

These calculations of differences were performed at each location with no distinction between tissues and the device materials.

B. Experimental Measurements

All experiments were performed using a 16 rung high pass birdcage body coil (MITS1.5, Zurich Med Tech, Zurich, Switzerland) with the same size used in the numerical simulations (ID = 746 mm, inner length = 570 mm, outer length = 650 mm) driven by two AN8102-08 RF power amplifiers (Analogic Co., Peabody, MA) for the quadrature driving. The electromagnetic field distributions of $||\mathbf{B_{xy}}||$ and $||\mathbf{E}||$ [7], [8] were measured by an electromagnetic field robotic measurement system (DASY system, DASY 5NEO, with the E-field probe ER3DV6 and the H-field probe H3DV7, Schmid & Partner Engineering AG, Zurich, Switzerland). The body coil was tuned at 63.5 MHz and the measurements of *S*-parameters related to the two input ports in Fig. 1(d) were approximately −12.6 dB (S11), −13.6 dB (S22), and −8.1 dB (S12) with the phantom and the breast expander device.

Four different 2-D regions, one transverse and three sagittal planes, were selected for the measurement. Specific location and size of the regions are

1) Transverse: *XY*-plane = 70 × 60 mm^2, offset *Z*-axis = −67 mm, the number of measurement points = 35 × 30,
2) First sagittal: *YZ*-plane = 70 × 140 mm^2, offset *X*-axis = 80 mm, the number of measurement points = 35 × 70,

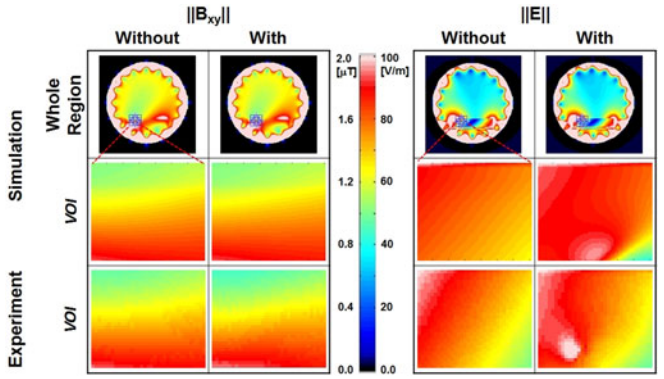

Fig. 2. Experimentally measured and related numerical simulations of $||\mathbf{B}_{\mathbf{xy}}||$ (first and second column) and $\|\mathbf{E}\|$ (third and fourth column) without (first and third column) and with (second and fourth column) the breast expander device located in the ASTM phantom and 1.5 T MITS body coil. The transverse plane images are shown with whole region (first row) and *VOI* (second and third row). Results are normalized for input forward power = 100 W.

3) Second sagittal: *YZ*-plane = 70 × 140 mm^2, offset *X*-axis = 180 mm, the number of measurement points = 35 × 70, and
4) Third sagittal: *YZ*-plane = 70×600 mm^2, offset *X*-axis = 0 mm, the number of measurement points = 35 × 120, [see Fig. 1(b) and (f)].

The origin was the center of the body coil, which is the same as the center of the ASTM phantom. All regions except the third sagittal plane were selected as close as possible to the breast expander device for the DASY system. The third sagittal plane was selected to measure the electromagnetic fields of the center slice for a reference. A linear interpolation was conducted during the postprocessing of measured data in MATLAB (the MathWorks, Inc., Natick, MA).

All experimental results were normalized to a forward input power = 100 W.

III. Results

The electromagnetic analysis showed a significant effect on $|\mathbf{B}_1^+|$ and SAR when the "expander" was present.

Fig. 2 shows the experimentally measured $||\mathbf{B}_{\mathbf{xy}}||$ and $||\mathbf{E}||$ without and with the breast expander device located in the ASTM phantom. Specifically, the measured maximum electric field was 114.1 V/m with the breast expander device (third row and fourth column), whereas the electric field at the same location was 77.3 V/m without the device (third row and third column). The corresponding numerical simulations were performed for the comparison.

Figs. 3 and 4 show the calculated $|\mathbf{B}_1^+|$ and $\mathrm{SAR}_{1\mathrm{g}}$ maps at 128 MHz in the ASTM phantom (see Fig. 3 and Table II) and in "Ella" (see Fig. 4 and Tables III–V) along a coronal plane, with $\Delta|\mathbf{B}_1^+|$ and $\Delta\mathrm{SAR}_{1\mathrm{g}}$ within the 2-D device *VoI*. The maps on the left correspond to the case without implant, the middle column correspond to the case with the device present, and the maps on the right correspond to an additional analysis using the silicone pouch instead of the metal and saline device. The pattern of changes in the EM fields caused by the introduction of the expander device was found

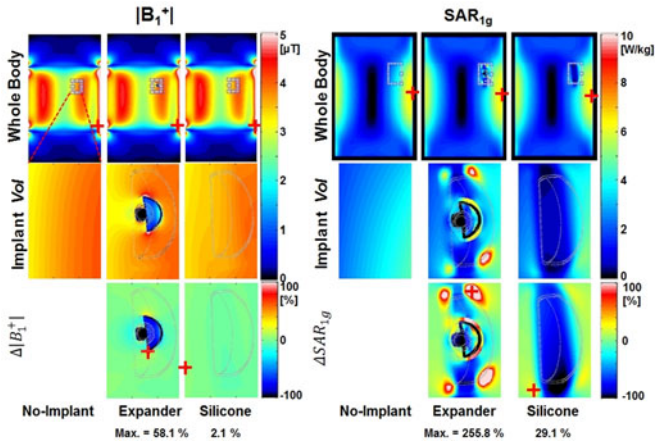

Fig. 3. (Top) $|\mathbf{B}_1^+|$ (left) and 1g-averaged SAR ($\mathrm{SAR}_{1\mathrm{g}}$, right) at 128 MHz using an ASTM phantom on the coronal plane containing the voxel with $\mathrm{SAR}_{1\mathrm{g-peak}}$ within the three-dimensional device volume-of-interest (*VoI*); (middle) zoomed image around the *VoI*; and (bottom) $\Delta|B_1^+|$ and $\Delta\mathrm{SAR}_{1\mathrm{g}}$ between the cases without and with the device [see (3) and (4)]. The white rectangular box in each figure of the first row indicates the device *VoI*. The maximum difference values within the *VoI* for both $|\mathbf{B}_1^+|$ or $\mathrm{SAR}_{1\mathrm{g}}$ are indicated by a red cross and numbers in the bottom row. Note that the position and value of maximum difference of $|\mathbf{B}_1{}^+|$ or $\mathrm{SAR}_{1\mathrm{g}}$ are not the same as the position and value of $|\mathbf{B}_1^+|_{\mathrm{peak}}$ or $\mathrm{SAR}_{1\mathrm{g-peak}}$. All the simulation results were normalized to a whole body averaged SAR ($\mathrm{SAR}_{\mathrm{WB}}$) equal to 4 W/kg (first-level-controlled operating mode). An outline of the device was added using a white color in second and third rows to show the location of the device.

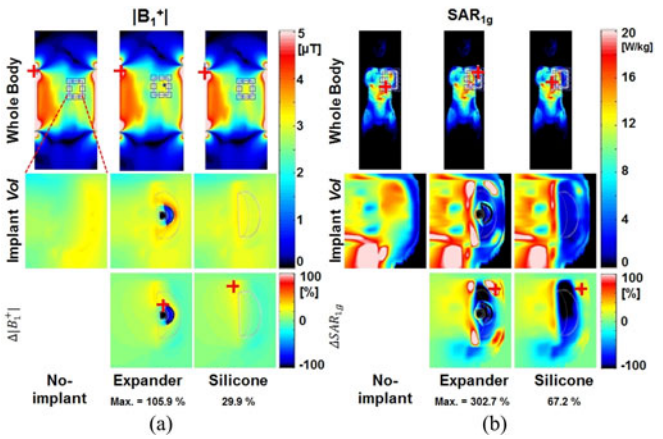

Fig. 4. $|\mathbf{B}_1{}^+|$ (a) and 1g-averaged SAR [$\mathrm{SAR}_{1\mathrm{g}}$, (b)] with "Ella" at 128 MHz with sternum landmark. Images are shown for the coronal plane containing the voxel with $\mathrm{SAR}_{1\mathrm{g-peak}}$ within the three-dimensional device volume-of-interest (*VoI*); (middle) zoomed image around the *VoI*; and (bottom) $\Delta|B_1^+|$ [see (3)] and $\Delta\mathrm{SAR}_{1\mathrm{g}}$ [see (4)] between the cases without and with the device. Results are normalized for $\mathrm{SAR}_{\mathrm{WB}} = 4$ W/ kg. Other parameters are the same as in Fig. 3.

TABLE II
SAR "Expander" vs. "Silicone" 610 mm Coil, ASTM Phantom at 128 MHz ($\mathrm{SAR}_{\mathrm{WB}} = 4$ W/ kg, $|\mathbf{B}_1^+|_{\mathrm{isocenter}} = 2.7\,\mu$T)

	Volume	No-implant	Expander	Silicone
$\mathrm{SAR}_{1\mathrm{g-peak}}$ [W/ kg]	*Whole*	16.3	31.9	16.4
	VoI	12.7	31.9	13.3
$\mathrm{SAR}_{10\mathrm{g-peak}}$ [W/ kg]	*Whole*	14.9	15.0	15.0
	VoI	12.5	14.5	13.1

TABLE III
SAR VS. LANDMARK POSITION—"EXPANDER" 64 MHZ (746 MM COIL) VS. 128 MHZ (610 MM COIL), $\mathrm{SAR_{WB}} = 4$ W/ KG, ELLA

	Volume	Shoulder		Heart		Sternum		Abdomen	
		64 MHZ	128 MHz	64 MHZ	128 MHz	64 MHZ	128 MHz	64 MHZ	128 MHz
$\mathrm{SAR_{1g-peak}}$ [W/ kg]	*Whole*	115	81.9	114	64.1	122	63.1	122	57.8
	VoI	114 (253%)*	55.8 (0%)*	113 (162%)*	43.6 (42%)*	79.6 (120%)*	58.1 (77%)*	41.4 (77%)*	33.3 (6%)*
$\mathrm{SAR_{10g-peak}}$ [W/ kg]	*Whole*	72.9	59.6	59.0	42.0	66.7	39.9	67.6	35.2
	VoI	49.0 (67%)*	38.1 (0%)*	48.5 (60%)*	22.3 (3%)*	34.5 (32%)*	21.6 (–4%)*	18.9 (14%)*	20.3 (0%)*
Dissipated Power [W]	*Whole*	334	297	325	269	364	252	241	257

*Percentage changes in brackets refer to $\Delta \mathrm{SAR_{Peak}}$ [see (5)].

TABLE IV
SAR VS. IMPLANT—"ELLA" AT 128 MHZ 610 MM COIL – STERNUM LANDMARK

	Volume	No-implant		Expander		Metal only		Saline only		Silicone	
		(A)	(B)	(A)	(B)	(A)	(B)	(A)	(B)	(A)	(B)
$\mathrm{SAR_{1g-peak}}$ [W/ kg]	*Whole*	46.9	63.6	46.1	63.1	46.8	63.6	46.3	62.9	46.6	63.3
	VoI	24.2	32.9	42.4	58.1	24.2	32.9	43.9	59.6	21.5	29.4
$\mathrm{SAR_{10g-peak}}$ [W/ kg]	*Whole*	29.6	40.2	29.1	39.9	29.6	40.2	29.3	39.8	29.4	40.0
	VoI	16.7	22.6	15.8	21.6	16.7	22.7	16.2	22.0	15.4	21.1

TABLE V
SAR VS. IMPLANT—"ELLA" AT 128 MHZ 750 MM COIL – STERNUM LANDMARK (A) $|\mathbf{B}_1^+| = 2\,\mu$T NOR. ($\mathrm{SAR_{WB}} = 3 \pm 0.1$ W/ KG) VS. (B) $\mathrm{SAR_{WB}} = 4$ W/ KG NOR.

	Volume	No-implant		Expander		Metal only		Saline only		Silicone	
		(A)	(B)	(A)	(B)	(A)	(B)	(A)	(B)	(A)	(B)
$\mathrm{SAR_{1g-peak}}$ [W/ kg]	*Whole*	104	131	94.2	131	103	131	94.1	130	94.0	131
	VoI	46.1	58.4	51.0	70.4	45.8	58.5	52.9	73.0	30.5	42.4
$\mathrm{SAR_{10g-peak}}$ [W/ kg]	*Whole*	60.9	77.1	55.3	76.4	60.4	77.1	55.3	76.3	55.2	76.9
	VoI	27.4	34.7	24.7	34.1	27.3	34.8	25.6	35.4	20.6	28.7

to be qualitatively similar for the phantom and Ella. The maximum $\Delta \mathrm{SAR_{1g}}$ and $\Delta \mathrm{SAR_{10g}}$ were found to be around the shell but not near the port. For SAR, the vicinity of the tapered regions showed focal increased values (256% for phantom). The results for the silicone device were qualitatively similar to saline but much more modest changes (256% vs. 29.1%) in $\Delta \mathrm{SAR_{1g}}$ (see Fig. 3). When comparing the results with the ASTM phantom vs. "Ella" in this plane, the maximum $\Delta|\mathbf{B}_1^+|$ was 58.1% vs. 106%, and the maximum $\Delta \mathrm{SAR_{1g}}$ was 256% vs. 303%, respectively. Conversely, the results obtained with the "silicone" showed a maximum $\Delta \mathrm{SAR_{1g}}$ of 29.1% (ASTM phantom) vs. 67.2% ("Ella"). Note that the position and the value of maximum $\Delta \mathrm{SAR_{1g}}$ are not the same as the position and the value of $\mathrm{SAR_{1g-peak}}$.

Simulations confirmed that SAR changes with the implant depended on frequency, coil, and landmark. Figs. 5 and 6 show $\mathrm{SAR_{1g}}$ calculated with the 750 mm coil at 64 MHz and the 610 mm coil at 128 MHz, respectively, with the four landmark positions. The values of $\Delta \mathrm{SAR_{1g}}$ were up to 653% (shoulder landmark, Fig. 5) at 64 MHz and up to 384% (abdomen landmark, Fig. 6) at 128 MHz. The localized increase of SAR in the *VoI* with respect to the increase of SAR over the entire body was strongly dependent on the landmark.

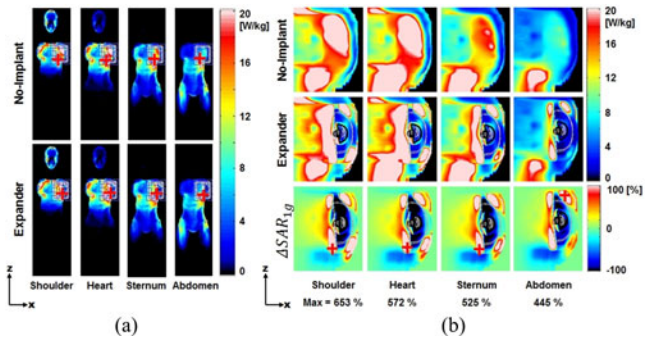

Fig. 5. $\mathrm{SAR_{1g}}$ at 64 MHz with the Ella model ("750 mm-ID coil") with four different landmark positions (i.e., shoulder, heart, sternum, and abdomen). [Left, (a)] Coronal maps over the whole body model in the plane with the highest $\mathrm{SAR_{1g-peak}}$ within the *VoI*. Results are shown for both the cases without ("no-implant") and with the breast tissue expander device ("Expander"). $\mathrm{SAR_{1g-peak}}$ within the selected plane is indicated by a red cross. [Right, (b)] Zoomed image within the *VoI*. The images show $\mathrm{SAR_{1g}}$ without and with the expander, and $\Delta \mathrm{SAR_{1g}}$. Results are normalized for $\mathrm{SAR_{WB}} = 4$ W/ kg. Other parameters are the same as in Fig. 3.

As shown in Table III, $\mathrm{SAR_{1g-peak}}$ in the *VoI* for the shoulder landmark position was 114 W/kg, with a 253% increase compared to the case without the implant; for this landmark, this value represented also $\mathrm{SAR_{1g-peak}}$ for the entire body.

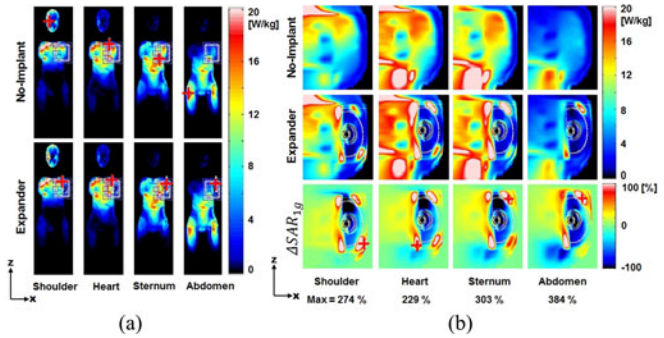

Fig. 6. $\mathrm{SAR_{1g}}$ at 128 MHz with the Ella model ("610 mm-ID coil") with four different landmark positions (i.e., shoulder, heart, sternum, and abdomen). [Left, (a)] Coronal view of the maps over the entire body model for the plane with the highest $\mathrm{SAR_{1g-peak}}$ within the *VoI* (box). Results are shown for both the cases without ("No-Implant") and with the breast tissue expander device ("Expander"). The $\mathrm{SAR_{1g-peak}}$ within the selected plane is indicated by a red cross. [Right, (b)] Zoomed image within the *VoI*. The images show $\mathrm{SAR_{1g}}$ without and with the expander, and $\Delta\mathrm{SAR_{1g}}$. Results are normalized for $\mathrm{SAR_{WB}} = 4$ W/ kg. Other parameters are the same as in Fig. 3.

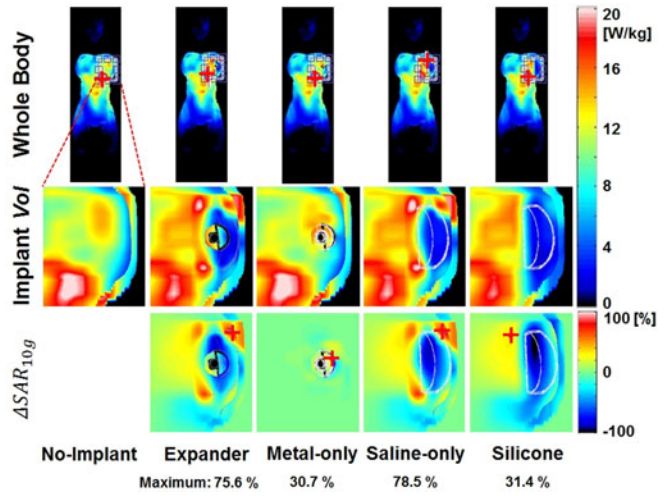

Fig. 7. $\mathrm{SAR_{10g}}$ at 128 MHz in a coronal plane having $\mathrm{SAR_{10g-peak}}$ within the three-dimensional device *VoI*; (middle) zoomed image within the *VoI*; and (bottom) difference between the cases without and with the device. Note that the position and value of maximum difference of $\mathrm{SAR_{10g}}$ are not the same as the position and value of $\mathrm{SAR_{10g-peak}}$. Other parameters are the same as in Fig. 3.

Conversely, for the abdomen landmark, $\mathrm{SAR_{1g-peak}}$ was 41.4 W/kg, with a 77% increase in the *VoI* compared to the case without the implant; however, this value was significantly less than $\mathrm{SAR_{1g-peak}}$ over the entire body (which was located near the breast expander device and was equal to 122 W/kg, see Fig. 5).

For all landmarks, the highest increase of SAR (i.e., $\mathrm{SAR_{1g}}$ and $\mathrm{SAR_{10g}}$) was observed at the interface between the elastomer wall and the breast tissue (see Figs. 5 and 6), whereas the SAR near the metallic port was lower, due to the shielding effect of the saline. This effect was confirmed by the analysis with additional implant models (i.e., "metal only," "saline only," "silicone"), (see Fig. 7 for the $\mathrm{SAR_{10g}}$ maps, similar profiles were present for the $\mathrm{SAR_{1g}}$ maps), which confirmed that the overall changes of SAR were caused by a combined SAR increase of the metallic port ("metal only") and the dielectric saline pouch ("saline only").

As shown in Table IV, the "expander" generated $\mathrm{SAR_{1g-peak}}$ of 42.4 W/kg at 128 MHz (for $|\mathbf{B_1^+}| = 2\,\mu$T normalization), similar to the value generated by the "saline only," i.e., 43.9 W/kg. For comparison, $\mathrm{SAR_{1g-peak}}$ in the *VoI* was 24.2 W/kg with "metal only" and 21.5 W/kg with "silicone." For the case of "silicone" and the 610 mm coil at 128 MHz, the sensitivity of the results for $\mathrm{SAR_{1g-peak}}$ with respect to the conductivity of the silicone [1] was 377%/S/m in the *VoI* (114%/S/m in the whole volume). Additionally, the sensitivity for $\mathrm{SAR_{10g-peak}}$ in the *VoI* was 150%/S/m and (26%/S/m in the whole volume).

IV. Discussion

An initial comparison with the literature was performed for the values of background SAR without the implant obtained with the body coil models used for this study. The ratio of $\mathrm{SAR_{10g-peak}}/\mathrm{SAR_{WB}}$ was significantly dependent on the coil diameter and length. The values were in the range of what has been reported in the literature with "Ella" [17], although a direct comparison is limited by different simulation conditions, such as location of the sources and grid resolution.

The high electrically conductive compartments of the breast expander device, i.e., the metallic port made of titanium ($\sigma = 2.33 \times 10^6$ S/ m, $\varepsilon_r = 1$) or samarium-cobalt ($\sigma = 116 \times 10^4$ S/ m, $\varepsilon_r = 1$), mainly affect the conduction current density ($\mathbf{J_c} = \sigma\mathbf{E}$ [A/ m^2], when $\mathbf{E}$ is the total electric field) rather than the displacement current density [$\mathbf{J_d} = j\omega\varepsilon_0\varepsilon_r\mathbf{E}$ [A/ m^2], when $j^2 = -1$, ω is the radian frequency [1/s], and ε_0 is the permittivity at free space (8.854×10^{-12} F/m)] [29], [30]. The ratios of $||\mathbf{J_c}||/||\mathbf{J_d}||$ for the titanium and samarium-cobalt are approximately 327×10^6 and 163×10^6, respectively. Conversely, the ratio of $||\mathbf{J_c}||/||\mathbf{J_d}||$ for dielectric compartments, i.e., saline ($\sigma = 0.47$ S/ m, $\varepsilon_r = 80$), is approximately 0.8. The total magnetic field and $|\mathbf{B_1^+}|$ are proportional to the sum of $\mathbf{J_c}$ and $\mathbf{J_d}$ as per Ampere's law. The sum of $||\mathbf{J_c}||$ and $||\mathbf{J_d}||$ for the saline, i.e., $1.04||\mathbf{E}||$, is much smaller than that of titanium, i.e., $2.33 \times 10^6||\mathbf{E}||$, or samarium-cobalt, i.e., $116 \times 10^4||\mathbf{E}||$; thus, the effect of the saline to the total magnetic field and $|\mathbf{B_1^+}|$ is much smaller than that of the metallic port. This is consistent with the results of Figs. 3 and 4 showing the dominant source of $|\mathbf{B_1^+}|$ variation is the metallic port, not saline.

Even though the dielectric compartment, i.e., saline, does not significantly affect the $|\mathbf{B_1^+}|$ variation in this study, it can significantly affect the $\mathbf{E}$ and SAR distribution through the partial shielding effect by generating an additional $\mathbf{E}$ which destructively interfere with the incident $\mathbf{E}$ generated by the RF coil [8], [31] (see Figs. 3–4 and 7). Similar results were obtained when modeling the device without the metallic component ("saline only") or even with the silicone implant ("silicone") (see also Tables IV and V). These results are in line with the shielding effect and the reshaping of the electric field due to the presence of a large insulator, discussed in the literature by Davis *et al.* [15].

Fig. 2 shows the experiment results and corresponding numerical simulations of $||\mathbf{B_{xy}}||$ and $||\mathbf{E}||$ without and with the

breast expander device. The measurements in the transverse plane showed that the biggest change of $||\mathbf{E}||$ (77.3 vs. 114.1 V/m) is due to the presence of the expander. Results of other regions had less difference (less than 10%) between with and without the breast expander device.

This is due to the restriction of the robotic arm with respect to the phantom. The experimental results in Fig. 2 showed hot spots of $\|\mathbf{E}\|$ due to the device. This is well matched with the corresponding numerical simulations. However, some discrepancies between experimental and numerical results are observed because of geometrical variation of the device during a fixation in the grid, simplification of the coil model, and error margin of the system including RF amplifiers and DASY system.

The DASY system allows measurement of the rms value of the amplitude of the electric and magnetic field but does not provide information about the phase. Thus, it was not possible to measure the values of $|\mathbf{B}_1^+|$, hence the normalization method of a forward input power $= 100$ W was used.

As shown in Table III, the extent of the localized increase of SAR in the *VoI* with respect to the increase of SAR over the entire body was strongly depending on the landmark-based position of the body model in the birdcage coil. Additionally, as shown in Tables IV and V, the extent of the localized increase of SAR in the *VoI* with respect to the increase of SAR over the entire body did not qualitatively depend on the type of normalization (i.e., $|\mathbf{B}_1^+|$ or $\mathrm{SAR_{WB}}$) or by the type of coil (610 vs. 750 mm) albeit the quantitative values were – as expected – different. Notably, when comparing the results between 610 vs. 750 mm coils, the background SAR without the implant was higher with the wider coil (e.g., $\mathrm{SAR_{1g-peak}}$ was 63.6 vs. 131 W/kg), which is consistent with previous research [32], [33]. In both cases, the peak values were outside the *VoI*. Thus, for the specific models used in this study, the effect of the implant did not seem to depend on the coil, possibly due to the specific anatomical location of the implant with respect to the coil.

As shown in Figs. 5 and 6, the $\mathrm{SAR_{1g}}$ and $\mathrm{SAR_{10g}}$ varied significantly with landmark position, which is consistent with previous studies [17], [18]. In Fig. 5, the position of $\mathrm{SAR_{1g-peak}}$ at 64 MHz was in the tissue near the device. The highest $\Delta\mathrm{SAR_{Peak}}$ for both $\mathrm{SAR_{1g}}$ and $\mathrm{SAR_{10g}}$ was with the shoulder landmark (see Table III). Conversely, the maximum $\Delta\mathrm{SAR_{1g}}$, not $\Delta\mathrm{SAR_{1g-peak}}$, was obtained at the abdomen landmark at 128 MHz-610 mm coil (see Fig. 6), likely because the breast tissue expander device for this landmark was close to the end ring of the coil, where high magnitude of electric fields is present [34]. Notably, the trend of the results for $\mathrm{SAR_{1g-peak}}$ did not necessarily correspond to the ones of $\Delta\mathrm{SAR_{1g}}$. For example, when comparing the results with the landmark position of sternum vs. abdomen, $\mathrm{SAR_{1g-peak}}$ decreased (see Table II) whereas the maximum $\Delta\mathrm{SAR_{1g}}$ increased (see Fig. 6).

The electromagnetic field variations due to the filling condition, i.e., full vs. half-full, were evaluated at 64 MHz using the ASTM phantom [5]. The result shows that the maximum 10g-averaged SAR of the half-full device within the volume of interest was decreased by 36% (15.0 vs. 9.6 W/kg) compared to 10g-averaged SAR of the full volume of the device. This is in line with the previous research [5] that showed temperature change between –33% (McGhan 67-133FX13, 500 ml) and +50% (McGhan 67-133SV13, 300 ml).

The results of this study are limited to the specific body models, device location, and orientation. Specifically, a single human body model based on a healthy female subject was implemented. Because the SAR distribution in the human body is a function of the size and the body mass composition (e.g., ratio of muscle vs. fat tissue), the results of this study may vary when evaluating a subject with higher/lower body mass index and muscle/fat composition. Also, the electromagnetic properties of the breast tissue were assigned as a breast fat ignoring the tissue of breast gland having different values [23]. This was due to the limitation of the used Ella model having one component of tissue in the breast region. Additionally, the study was performed with a single orientation and size of the breast expander, and single tune condition, which could potentially alter the results since the RF-induced heating is a function of the size and orientation of the device. Also the device was located on the left side of the human model, which showed high background SAR, to provide a sufficient level of electric field enhancement. Finally, the study did not address all of the aspects of MR safety for breast tissue expander devices (e.g., safety with respect to force/torque) which were beyond the scope of the study.

V. Conclusion

In conclusion, numerical simulation results of RF safety evaluation for the breast tissue expander device are presented using a female human anatomical model, two different body coils, four different landmarks, and two different operating frequencies of 64 and 128 MHz. SAR alterations depended on the specific landmark, but not on the type of normalization used. There were significant increases of $\mathrm{SAR_{10g}}$ and $\mathrm{SAR_{10g-peak}}$ with the addition of the breast tissue expander device up to 102% at 128 MHz and 444% at 64 MHz within the device *VoI*. However, $\mathrm{SAR_{10g-peak}}$ in the volume surrounding the device was still less than 85% of $\mathrm{SAR_{10g-peak}}$ over the whole body region at any landmark positions in this study. The increases in SAR are relatively modest and not enough to present a significant heating risk in tissue.

Acknowledgment

The authors thank Dr. D. Shrivastava for valuable technical discussion. The mention of commercial products, their sources, or their use in connection with material reported herein is not to be construed as either an actual or implied endorsement of such products by the Department of Health and Human Services.

References

[1] American Cancer Society 2011–2012, Breast Cancer. [Online]. Available: http://www.cancer.org/acs/groups/content/@epidemiologysurveilance/documents/document/acspc-030975.pdf.

[2] M. Morrow *et al.*, "Surgeon recommendations and receipt of mastectomy for treatment of breast cancer," *J. Amer. Med. Assoc.*, vol. 302, no. 14, pp. 1551–1556, Oct. 2009.

[3] Food and Drug Administration (FDA). [Online]. Available: http://www.accessdata.fda.gov/scripts/cdrh/cfdocs/cfPMN/pmn.cfm.

[4] K. B. Baker, J. A. Nyenhuis, G. H. Bsee, A. R. Rezai, J. A. Tkach, and F. G. Shellock, "Neurostimulation systems: Assessment of magnetic field interactions associated with 1.5- and 3- tesla MR systems," *J. Magn. Reson. Imag.*, vol. 21, pp. 72–77, 2005.

[5] M. B. Nava *et al.*, "Effects of the magnetic resonance field on breast tissue expanders," *Aesthetic Plast. Surg.*, vol. 36, no. 4, pp. 901–907, 2012.

[6] A. Razjouyan, B. S. Park, T. Key, L. Angelone, T. Woods, and S. Rajan, "MRI safety testing of breast tissue expanders," presented at the *ISMRM MR Safety Workshop*, 2014, Paper P141.

[7] B. S. Park, A. G. Webb, and C. M. Collins, "A method to separate conservative and magnetically-induced electric fields in calculations for MR microscopy," *J. Magn. Reson.*, vol. 199, pp. 233–237, 2009.

[8] B. S. Park, T. Neuberger, A. G. Webb, D. C. Bigler, and C. M. Collins, "Faraday shields within a solenoidal coil to reduce sample heating: Numerical comparison of designs and experimental verification," *J. Magn. Reson.*, vol. 202, pp. 72–77, 2010.

[9] *Particular Requirements for the Safety of the Magnetic Resonance Equipment for Medical Diagnosis*, Std. IEC-60601-2-33, 2010.

[10] H. S. Ho, "Safety of metallic implants in magnetic resonance imaging," *J. Magn. Reson. Imag.*, vol. 14, pp. 472–477, 2001.

[11] E. Mattei *et al.*, "Temperature and SAR measurement errors in the evaluation of metallic linear structures heating during MRI using fluoroptic probes," *Phys. Med. Biol.*, vol. 52, no. 6, pp. 1633–1646, 2007.

[12] B. S. Park, M. J. Lizak, L. M. Angelone, and S. S. Rajan, "Real time MR thermometry using Tm-DOTMA," *J. Electromagn. Anal. Appl.*, vol. 7, pp. 115–125, 2015.

[13] W. Kainz, "MR heating tests of MR critical implants," *J. Magn. Reson. Imag.*, vol. 26, pp. 450–451, 2007.

[14] F. G. Shellock, "Comments on MR heating tests of critical implants," *J. Magn. Reson. Imag.*, vol. 26, pp. 1182–1185, 2007.

[15] P. L. Davis, C. Shang, L. Talagala, and A. W. Pasculle, "Magnetic resonance imaging can cause focal heating in a nonuniform phantom," *IEEE Trans. Biomed. Eng.*, vol. 40, no. 12, pp. 1324–1327, Dec. 1993.

[16] F. G. Shellock, *Reference Manual for Magnetic Resonance Safety, Implants, and Devices*, 2015 ed. Fitchburg, MA, USA: MAGMEDIX, 2015.

[17] M. Murbach, E. Neufeld, W. Kainz, K. P. Pruessmann, and N. Kuster, "Whole-body and local RF absorption in human models as a function of anatomy and position within 1.5T MR body coil," *Magn. Reson. Med.*, vol. 71, no. 2, pp. 839–845, 2014.

[18] M. Murbach et al., "Local SAR enhancements in anatomically correct children and adult models as a function of position within 1.5 T MR body coil," *Prog. Biophys. Mol. Biol.*, vol. 107, pp. 428–433, 2011.

[19] K. Yee, "Numerical solution of initial boundary value problems involving Maxwell's equations in isotropic media," *IEEE Trans. Antennas Propag.*, vol. 14, no. 3, pp. 302–307, May 1966.

[20] A. Taflove and S. C. Hagness, *Computational Electrodynamics : The Finite-Difference Time-Domain Method*, Boston, MA, USA: Artech House, 2000, p. 852.

[21] A. Christ *et al.*, "The virtual family—Development of surface-based anatomical models of two adults and two children for dosimetric simulations," *Phys. Med. Biol.*, vol. 55, pp. 23–38, 2010.

[22] Material properties. [Online]. Available: <http://www.matweb.com/search/DataSheet.aspx?MatGUID=fa437f4b5fe846c892a907023a38156d; [Online]. Available: http://www.matweb.com/search/datasheet.aspx?matguid=6ce20df379e64f28b0c7aa7332ec50f0; (a) Samarium-Cobalt. [Online]. Available: http://en.wikipedia.org/wiki/Samarium%E2%80%93cobalt_magnet. (b) Silicone. [Online]. Available: http://en.wikipedia.org/wiki/Relative_permittivityc. (c) Magnet. [Online]. Available: http://www.arnoldmagnetics.com/uploadedFiles/Products/Samarium_Cobalt/Recoma_Grade_pdfs/Recoma%20Combined%20-%20140527.pdf.

[23] S. Gabriel, R. Lau, and C. Gabriel, "The dielectric properties of biological tissues: II. Measurements in the frequency range 10 Hz to 20 GHz," *Phys. Med. Biol.*, vol. 41, pp. 2251–2269, 1996.

[24] E. Lucano *et al.*, "Assessing the electromagnetic fields generated by a radiofrequency MRI body coil at 64MHz: Defeaturing vs. accuracy," *IEEE Trans. Biol. Eng.*, vol. 63, no. 8, pp. 1591–1601, Aug. 2016.

[25] D. T. B. Yeo, Z. Wang, W. Loew, M. W. Vogel, and I. Hancu, "Local specific absorption rate in high-pass birdcage and transverse electromagnetic body coils for multiple human body models in clinical landmark positions at 3T," *J. Magn. Reson. Imag.*, vol. 33, pp. 1209–1217, 2011.

[26] *Standard Test Method for Measurement of Radio Frequency Induced Heating on or Near Passive Implants During Magnetic Resonance Imaging*, Std. ASTM-F2182, 2011. [Online]. Available: http://www.astm.org/Standards/F2182.htm.

[27] P. A. Hasgall *et al.*, "IT'IS database for thermal and electromagnetic parameters of biological tissues," Ver. 3.0, 2015. Doi: 10.13099/VIP21000-03-0. [Online]. Available: www.itis.ethz.ch/database.

[28] C. M. Collins, S. Li, and M. B. Smith, "SAR and B1 field distributions in a heterogeneous human head model within a birdcage coil," *Magn. Reson. Med.*, vol. 40, pp. 847–856, 1998.

[29] C. A. Johnk, *Engineering Electromagnetic Fields and Waves*, 2nd ed. Hoboken, NJ, USA: Wiley, 1998, pp. 35–36.

[30] C. M. Collins and M. B. Smith, "Signal-to-noise ratio and absorbed power as functions of main magnetic field strength, and definition of "90 degrees" RF pulse for the head in the birdcage coil," *Magn. Reson. Med.*, vol. 45, pp. 684–691, 2001.

[31] B. S. Park, S. S. Rajan, J. W. Guag, and L. M. Angelone, "A novel method to decrease electric field and SAR using an external high dielectric sleeve at 3T Head MRI: numerical and experimental results," *IEEE Trans. Biol. Eng.*, vol. 62, no. 4, pp. 1063–1069, Apr. 2015.

[32] E. Neufeld, M. C. Gosselin, M. Murbach, A. Christ, E. Cabot, and N. Kuster, "Analysis of the local worst-case SAR exposure caused by an MRI multi-transmit body coil in anatomical models of the human body," *Phys. Med. Biol.*, vol. 56, pp. 4649–4659, 2011.

[33] J. W. Hand, Y. Li, E. L. Thomas, M. A. Rutherford, and J. V. Hajnal, "Prediction of specific absorption rate in mother and fetus associated with MRI examinations during pregnancy," *Magn. Reson. Med.*, vol. 55, pp. 883–893, 2006.

[34] B. S. Park, S. S. Rajan, C. M. Collins, and L. M. Angelone, "Analysis of conservative and magnetically induced electric fields in a low-frequency birdcage coil," *J. Electromagn. Anal. Appl.*, vol. 5, pp. 271–280, 2013.

Bu S. Park received the B.S. degree in biomedical engineering from Kon-Kuk University (*summa cum laude*), Seoul, South Korea, in 1996, and the Ph.D. degree in bioengineering from the Pennsylvania State University, State College, PA, USA, in 2009.

From 1998 to 2005, he served as an RF and System Engineer in Medison and Medinus Co., Ltd., MRI Division, South Korea. From 2009 to 2011, he completed a post-doctoral fellowship with the National Institutes of Health. Since 2011, he has been a Research Fellow with the Food and Drug Administration, Silver Spring, MA, USA. His research interests include the use of computational modeling and experimental measurements aimed to design RF coils for MRI and evaluate RF safety for patients with medical devices.

Amir Razjouyan received the B.S. and M.S. degrees in electrical engineering from the Catholic University of America, Washington, DC, USA, in 2015.

He had been an ORISE Research Fellow and is currently a Lead Reviewer with the Food and Drug Administration, Silver Spring, MA, USA.

Leonardo M. Angelone received the Laurea in electronic engineering from the University of Rome "La Sapienza," Rome, Italy, in 2001. In 2008, he received the Ph.D. degree in biomedical engineering from Tufts University, Medford, MA, USA.

He is a Research Biomedical Engineer in the Office of Science and Engineering Laboratories, Center of Devices and Radiological Health, U.S. Food and Drug Administration (FDA), Silver Spring, MA, USA. He has authored more than 100 peer-reviewed journal articles and conference proceedings. He completed a Research Fellowship in the Department of Radiology of the Massachusetts General Hospital, Harvard Medical School. Prior to joining the FDA, he was a Consultant in the Research and Development Department, Surgical Products Division, Hologic, Inc. His research interests include the assessment of energy deposition and heating induced in the human body by medical devices using electromagnetic energy.

Brent McCright received the Ph.D. degree in oncological sciences from the University of Utah, Salt Lake City, UT, USA, in 1997. He studied developmental biology and mammalian genetics during his postdoctoral fellowship research at the Jackson Laboratory, Bar Harbor, ME, USA.

He joined the Division of Cellular and Gene Therapies, Office of Cellular, Tissue, and Gene Therapies, Center for Biologics Evaluation and Research, Food and Drug Administration, Silver Spring, MA, USA, in 2002. He reviews INDs and works on policy development for cellular therapies. In addition, his lab investigates the function of key signaling molecules during organogenesis and tissue repair using a variety of *in vivo* imaging tools including MRI. The goal of his current research is to identify molecules that may be useful in predicting the effectiveness of cellular therapies.

Sunder S. Rajan received the Ph.D. degree in chemistry from the University of Chicago, Chicago, IL, USA, in 1984.

From 1984 to 1987, he was a Post-Doctoral Fellow in the Johns Hopkins University School of Medicine, Radiology Department, working in the field of *in vivo* NMR. He subsequently was an Assistant Professor in the Department of Radiology, Georgetown University Hospital, until 1996. During this period, he was involved in MRI research. From 1996 to 2006, he worked in the industry participating in clinical research and product development of contrast agents. He is currently a Researcher in the Center of Devices and Radiological Health, Food and Drug Administration, Silver Spring, MA, USA. His current research interests include MRI technology, safety aspects of MRI, and MRI-based biomarkers.